# Superelasticity by Reversible Variant Reorientation in a Ni-Mn-Ga Microwire with Bamboo Grains

Z.L. Wang[1,2], P. Zheng[1], Z.H. Nie[2], Y. Ren[3], Y.D. Wang[4], P. Müllner[5], D.C. Dunand[1,*]

[1] Department of Materials Science & Engineering, Northwestern University, Evanston, IL 60208, USA
[2] School of Materials Science & Engineering, Beijing Institute of Technology, Beijing 100081, China
[3] X-Ray Science Division, Argonne National Laboratory, Argonne, Illinois 60439, USA
[4] State Key Laboratory of Advanced Metals and Materials, University of Science and Technology Beijing, Beijing 100083, China
[5] Department of Materials Science & Engineering, Boise State University Boise, ID 83725, USA

*Corresponding author: dunand@northwestern.edu

**Abstract**

The link between microstructure and mechanical properties is investigated for a superelastic Ni-Mn-Ga microwire with 226 μm diameter, created by solidification via the Taylor method. The wire, which consists of bamboo grains with tetragonal martensite matrix and coarse γ precipitates, exhibits fully reversible superelastic behavior up to 4% tensile strain. Upon multiple tensile load-unload cycles, reproducible stress fluctuations of ~3 MPa are measured on the loading superelastic stress plateau of ~50 MPa. During cycles at various temperatures spanning -70 to 55 $^{o}$C, the plateau stress decreases from 58 to 48 MPa near linearly with increasing temperature. Based on in-situ synchrotron X-ray diffraction measurements, we conclude that this superelastic behavior is due to reversible martensite variant reorientation with lattice rotation of ~13$^{o}$, occurring consecutively at various locations along the wire during load-unload loops, leading to the reproducible stress fluctuations on the stress plateau. The strain recovery during unloading is attributed to the internal stress generated by the γ precipitates impeding the motion of the twin boundaries. The temperature dependence of the twining stress is related to the change in tetragonality of the martensite, as measured by X-ray diffraction.

**Keywords:** $Ni_2MnGa$, size effect, superelasticity, shape-memory effect, twinning, oligocrystalline materials.

## 1. Introduction

Ni-Mn-Ga alloys are the most studied of ferromagnetic shape memory alloys because of their large magnetic-field-induced strain (MFIS), which is achieved through the motion of the twin boundary, i.e., the reorientation of the martensite variants. The maximum reported MFIS is ~6% [1], ~10% [2], and ~12% [3] for five-layered modulated (5M), seven-layered modulated (7M) and non- modulated (NM) martensite, respectively. The very large MFIS, which opens potential applications for actuators, sensors and energy harvesters, is attained in single crystals but is near zero in polycrystalline materials because of constraints by grain boundaries on the motion of twin interface [4]. Dunand and Müllner proposed that these constraints can be reduced significantly when the grain size becomes comparable to one or more characteristic sample sizes (e.g., film thickness, wire or strut diameter, ribbon width, particle diameter), so that grains become partially surrounded by free space [5]. This approach has been demonstrated in polycrystalline Ni-Mn-Ga fibers [6] and foams [7] for which 1-8.7 % MFIS has been achieved.

Various researchers have recently studied Ni-Mn-Ga wires. Gómez-Polo et al. [8] prepared wires by rotating water bath melt spinning and observed coexistence of austenite and the 7M and 5M martensites. Zhukova et al. [9-15] prepared glass-coated wires by the Taylor method for Ni-Mn-Ga and Ni-Mn-In/Ni-Co-Mn-In alloys and investigated the effect of the internal stress between the metallic core and the glass sheath on the microstructure, phases and magnetic properties. Qian et al. [16] created superelastic austenitic $Ni_{49.9}Mn_{28.6}Ga_{21.5}$ wires with fine grains by melt extraction; on loading, the plateau stress for stress-induced martensitic transformation increases from 17 to 150 MPa with increasing temperature from 18 to 33 ºC, following the Clausius–Clapeyron relationship, with a slope of 8.7 MPa/ºC. Zhang et al. [17] achieved superelasticity in austenitic $Ni_{54.0}Mn_{24.1}Ga_{21.9}$ wires created by the Taylor method with reversible strains of up to 11.2% and plateau stress for stress-induced martensitic transformation of 115 MPa. Liu et al. [18] studied the effect of Ga substitution by Fe in melt-extracted Ni-Mn-Ga(Fe) wires on the thermal and magnetic (but not mechanical) properties. Recently, we created Taylor wires with composition of $Ni_{54.1}Mn_{26.2}Ga_{19.7}$ and martensitic bamboo grains, which, under an externally applied tensile stress, exhibit superelastic behavior with a twinning stresses of 22–30 MPa and recoverable tensile strains up to 3.5%, which was attributed to reversible intermartensitic transformation [19]. A 1 T magnetic field caused the wire to bend to a surface strain of 1.5%, and during field rotation, the wire deflected back and forth by reversible twinning, an effect called magnetic-torque-induced bending (MTIB). Further investigation of the relative importance of MFIS and MTIB has been recently carried out in monocrystalline, martensitic Ni-Mn-Ga beams (with a square 1x1 $mm^2$ cross section and length varying between 2 and 10 mm) subjected to a rotating magnetic field [20].

In the present article, a Ni-Mn-Ga Taylor wire, with 226 μm diameter and bamboo

grains, is studied during multiple superelastic tensile load-unload cycles. Mechanical testing, metallography and *in-situ* synchrotron X-ray diffraction reveal that superelasticity is due to reversible martensitic variant reorientation in the bamboo grains containing non-twining inclusion, together with lattice rotation.

## 2. Experimental procedures

### 2.1 Wire preparation

Ni-Mn-Ga button ingots with nominal chemical composition $Ni_{50}Mn_{28.6}Ga_{21.4}$ were prepared by arc-melting of high-purity elements. The button ingots were re-melted and cast into 7 mm diameter rods in copper mold. From these rods, wires with diameters ranging from 90 to 400 μm were cast by the Taylor method using a custom-made instrument. The process is described in Ref. [18] and is summarized briefly here. A cast rod is placed in a 8 mm diameter pyrex tube under Ar cover gas, induction-heated up to melting at ~1150 ºC and drawn in the liquid state within the softened pyrex tube into a thin, pyrex-coated wire under fast solidification conditions provided by natural cooling in ambient air, followed by quenching in sand. One wire was selected, with 226 μm diameter. The as-drawn wire with its glass sheath was sealed into a quartz capsule under low vacuum and homogenized at 1050 for 1 h and aged at 700 ºC for 12 h to induce grains growth leading to a bamboo-grain structure. The glass sheath was removed by grinding the wire gently on fine sand paper. The wire was cut into 25 mm length, and a small segment at its end was cut, metallographically prepared (including etching using Marble's reagent made up of 50 ml $H_2O$, 50 ml HCl and 10 g $CuSO_4$), and imaged via optical and scanning electron microscope (SEM, Hitachi S-3400N) with its chemical composition obtained by energy dispersive spectroscopy (EDS).

### 2.2 Tensile tests

The wire tensile properties were measured using a dynamical mechanical analyser (DMA, Q800 of TA Instruments). To avoid breaking the wire due to stress concentrations during direct gripping, gripping was performed on tabs consisting of two epoxy/glass composite squares glued onto a piece of cardboard by double-sided adhesive tape. The wire was glued at both its ends to the tabs with epoxy resin, creating a tensile gauge with 15 mm length. After gripping the wire, the cardboard was cut off by the blade. Tensile deformation was carried out at a rate of ~1 μm/s under deformation control. Strain was measured by cross-head displacement with a high-resolution linear optical encoder with a displacement resolution of 1 nm. Load was measured with a resolution of $10^{-4}$ N via a load cell.

### 2.3 In-situ synchrotron high-energy X-ray diffraction

Combined tensile testing and in-situ synchrotron high-energy X-ray diffraction was

conducted at the 11-ID-C beamline of the Advanced Photon Source (APS) at Argonne National Laboratory (Argonne, IL). A schematic illustration of the experiment is shown in Fig. 1. A custom tensile instrument was used to apply deformation and the load was recorded by a load cell (LCFD-5, Omega) while strain was measured via cross-head displacement. During the tensile test, the cross-head was stopped at 11 loading points (at strains of 0 to 3.33%) and 6 unloading points (at strains of 0 to 3.33%). At each applied strain, the monochromatic x-ray beam ($1\times1$ $mm^2$ size and 0.111650 Å wavelength) was transmitted through the wire and a diffraction pattern was collected by a 2-dimensional (2D) detector. At each applied strain, 15 diffraction patterns were collected to cover the entirety of the 15 mm gauge by translating the wire in 1 mm steps. The geometry for the diffraction is described by the coordinates system (Fig. 1): LD corresponds to the loading direction and TD to the transverse direction during the uniaxial tensile test. During collection of diffraction data, the wire was rotated in the range of ±7º to make more points in the reciprocal lattice tangent with the Ewald sphere, i.e., to collect more diffraction information. The 2D diffraction data were further integrated into 1D diffraction data (intensity versus 2θ graphs) by the Fit2D software.

Furthermore, xxxxthe diffraction patterns were collected for one segment at various temperatures cooling from 177 to 27 ºC. The wire was subjected to the variable heating/refrigerant flow regulated by the heating/cooling gun to obtain different temperatures.

## 3. Experimental results

### 3.1 Microstructure and phases

Fig. 2(a) shows the diameter and the surface condition of the wire after removal of the pyrex coating. Fig. 2(b) shows the fracture structure of the cross section at one end of the wire, showing cleavage indicative of brittle fracture. Coarse, elongated precipitates, identified as the γ phase by diffraction (as described later), are observed after polishing and etching a small section of the wire end, as shown in Fig. 2(c). Martensite plates (labelled M), visible as the fine parallel features in Fig. 2(c), span the whole cross-section, demonstrating that the grain size of the austenitic parent phase is comparable to the wire diameter, i.e., that a bamboo grain structure is present. Some micro-cavities (micro-holes labelled H) are also observed on the surface, which may be related to shrinkage during dendritic solidification. Micrographs of the etched longitudinal cross-sections of a small section of the wire end are shown in Figs. 2(d) and (e). The γ precipitates, with a 9% area fraction, show a growth direction which is nearly perpendicular to the longitudinal direction of the wire, i.e., in the direction of the heat flow when rapid solidification occurred. The precipitates appear mainly at one side of the wire, which may have been the nucleation side when the liquid wire solidified after contact with sand just after wire drawing. Figs. 2(d) and (e) also show that most martensite plates form a ~10º angle with the longitudinal direction of the wire (marked by the dotted line), with other martensite plates perpendicular to it.

Similar morphology was reported in magnetron sputtered single crystal Ni-Mn-Ga thin films, where the martensite plates intersect at an angle of 90º [21]. No grain boundaries is observed in all the longitudinal metallography for the whole piece. The chemical composition is determined by EDS for the phases. Four different measurement areas were selected and the average compositions are $Ni_{71\pm0.9}Mn_{7\pm1.2}Ga_{22\pm0.8}$ for the γ phase and $Ni_{60\pm0.8}Mn_{24\pm1.4}Ga_{16\pm1.2}$ for the martensite. Compared to the chemical composition of the ingot, substantial losses of Mn and Ga occured by evaporation during the melting of the ingot.

Two representative diffraction patterns at two different positions along the unstressed wire are shown in Fig. 3 for volumes with and without γ phase. The crystal structure for the martensite is identified as non-modulated tetragonal with a=3.81 Å, c=6.61 Å. The coarse γ phase can be indexed to a face-centered cubic structure with a=3.86 Å by the diffraction results, larger than a=3.618 Å in the previous report [22] due to the different chemical composition. The weak peaks correspond to the (200) and (220) of the γ phase in Fig. 3(a). A small amount of residual austenite can also be detected.

### 3.2 Mechanical properties

All tensile tests were performed on the same wire, which remained unfractured after about 30 cycles. Fig. 4(a) shows load-unload tensile stress-strain curves for maximum applied strains of 3, 4 and 5%. After elastic loading, a long plateau is reached at an applied strain of ~0.8%, which is typical of superelastic behavior such as stress-induced transformation from austenite to martensite in NiTi alloy. When unloading, the stress drops elastically at first before remaining constant at a lower stress plateau. For applied strains of 3 and 4%, the strain is near fully recoverable. For a 5% applied strains, a second elastic range occurs beyond 4% strain, and a residual strain of 0.4% is present after unloading. Stress fluctuations occur in both the upper and lower plateaus and are reproducible in each of the three loops. As the wire consists of tetragonal martensite, no stress-induced transformation is expected, and the plateau can be attributed to reorientation of variants, i.e.,the motion of the twinning boundary between variants, rather than martensitic or intermartensitic transformations. To verify that the fluctuations are true and reproducible, 8 cyclic tensile tests up to 2% strain were performed, as shown in Fig. 4(b) where the curves are shifted on the strain axis to provide better visibility. All 8 stress-strain curves are near identical in the number and magnitude of the stress fluctuations in the two plateaus.

The effect of temperature on the tensile properties was studied by carrying out tests at various temperatures, heating up from -70 to 55 ºC, as shown in Fig. 4(c). On loading, the upper stress plateau (or equivalently the critical stress defined as the maximum stress for the first fluctuation on the plateau) decreases linearly with increasing temperature. On unloading, the stress for the lower plateau increase accordingly. As result, the hysteresis which is associated with energy dissipation during the

load-unload cycle, decreases with increasing temperature. The temperature dependence of the critical stress is shown in Fig. 4(d). This superelastic temperature dependence is opposite to that observed in polycrystalline superelastic $Ni_{49.9}Mn_{28.6}Ga_{21.5}$ wire prepared by melt extraction [15], where the loading plateau stress decreases when decreasing the temperature towards the transformation temperature, indicating the different origin of superelasticity in the present Ni-Mn-Ga wire.

### 3.3 In-situ synchrotron X-ray diffraction

The stress-strain curve recorded during the in-situ X-ray diffraction is shown in Fig. 5. Between the strain range of 0-0.83%, only the stress/strain values for the target applied strain were recorded. The red dots on the curve represent the applied strain at which deformation was interrupted and 15 diffraction patterns (labelled 1-15 in Fig. 5) were collected along the full length of the wire. For the first measurement at zero strain, a tensile stress of ~8 MPa was applied to straighten the wire. The maximum applied strain was ~3.3% and the residual strain upon full unloading was ~0%.

Comparing all the diffraction patterns for segments 1-15 over the whole load-unload experiment, patterns evolve mostly over segments 7-10, while patterns for the other segments remain mostly unchanged throughout the load-unload loop. Thus, it can be concluded that anelastic deformation is mainly located in the center of the wire. Patterns for segment 7-10 before loading, at the maximum applied strain and after unloading are compared in Fig. 6. Laue spots represent the diffraction information of the various martensite variants. Fig. 6 shows that the patterns are the same before loading and after unloading. At the maximum strain, the patterns however show clear changes. For example, when loading from 0 to 3.33%, the partial rings for the $(004)_T$ and $(220)_T$ peaks transform into single spots and become less intense (for $(004)_T$) and they return to their original state after unloading from 3.33 to 0%, as marked with a red box for segment 7 in Fig. 6. Thus, it can be concluded that segments 7-10 consisted of a large grain containing multi-variants which twin into a near-single variant under the applied strain of 3.33%. When the load is removed, the diffraction patterns recover the multi-variant features present initially, demonstrating that strain recovery is paralleled by crystallographic reversibility.

The diffraction patterns for segments 7-10 on the upper plateau fluctuations are shown in Fig. 7 for five strains (marked on the stress-strain curve of Fig. 5), including a stress maximum at 1.2 and 3.0%. The colored frames in Fig. 7 highlight the pairs of diffraction patterns showing change, between which variant reorientation thus occurred. It is apparent that, for each of the four segments, variants reorientation takes place at different applied strain intervals, e.g., 1.2-1.73% for segment 9 and 3-3.33% for neighboring segment 10. This is indicative of a non-uniform deformation process along the wire.

To investigate the relationship between the lattice parameters and the twinning stress, 1D diffraction curves created by integrating the 2D diffraction pattern are fitted by the Lebail method using the EXPGUI software package [23] and the unit-cell lattice parameters, a and c, are determined (as reported earlier, a=3.81 Å, c=6.61 Å at ambient temperature). The results for an experiment performed by cooling from 177 to 27 ºC are reported in Fig. 8 showing the lattice parameter thermal strains, $\Delta a/a$ and $\Delta c/c$. It is apparent from this figure that the unit cell undergoes anisotropic thermal changes as the value of a decreases while that of c increases during cooling. Correspondingly, the tetragonality, defined by the ratio $c/\sqrt{2}a$, increases with decreasing temperature, as shown in Fig. 9(b). This figure also shows the volumetric thermal strain, defined as $\Delta V/V$ (where the unit cell volume is $V=a^2.c$), corresponding to a volumetric contraction during cooling with a coefficient of $60\times10^{-6}$ $K^{-1}$ averaged between 177 and 27 ºC.

## 4. Discussion

### 4.1 Structure evolution during tensile deformation

Based on the Bain model, the tetragonal unit cell for martensite can be described as a distortion of the $L2_1$ austenitic parent phase, i.e.,one axis is stretched and the other two are shrunk. The diffraction patterns cover the diffraction information of three domains, each of which consists of a pair of variants in twinning relationship, shown in Fig. 9(a); they are marked by (M+, T1) (M-, T2) and (V1, ?) [24-26], where M, T and V represent the variants with c axis pointing towards the LD, TD and beam directions, respectively. The + subscript denotes the counterclockwise rotation direction related to the intermediate position between M+ and M-. As the diffraction information, i.e.,Laue spot, of the variant oriented in twinning relationship with V1 is not detected, it is denoted by a question mark. By measuring the angles directly on the diffraction pattern on Fig. 9(a), the misorientation angle between M+ and M- is determined to be $\varphi$= ~13º and that between T1 and T2 to be $\psi$= ~8º, which is in reasonable agreement with the equation:

$$\varphi/2+\psi/2= 2\arctan(c/a)-90^{\circ} \quad (1)$$

as arctan(c/a) is equal to ~50.9º, using values for c and a reported earlier.

During straining, as shown in the pattern on the right of Fig. 9(a), the variants reorientat, i.e., detwinning occurs by the motion of the twin boundary between variants. As a result, the favorably orientated M+ and M-, variants grow at the expense of the T1 and T2 variants, respectively, corresponding to the intensity of the (004) peak in red circles decreasing while that of (220) peak increases in the transverse direction [27]. Simultaneously, a rigid lattice rotation occurs as measured by the reduction of the misorientation angle $\varphi$ between M+ and M- from 13º to ~0º and increase of $\psi$ between T1 and T2 from 8º to 21º. A schematic illustration

describing the process at the atomic scale is shown in Fig. 9(b).

### 4.2 Mechanism for fluctuations and superelasticity

The reorientation process, which is controlled by the detwinning dislocation moving on successive twin planes (i.e.,the movement of twin boundaries), takes place only when the external load approaches the twinning stress. Probably because of the nickel-rich concentration of the wire, the observed plateau stress, ~50 MPa, is much higher than the twinning stresses (~3 MPa) reported for near-stoichiometric $Ni_2MnGa$ which are sufficiently low to permit magnetic-field induced twinning [1-2][28]. Once twin boundaries become mobile and start to propagate, the internal stress is reduced and less energy is required for their further propagations. Thus, each of the stress peaks on the plateau corresponds to the maximum stress required to initiate local detwinning. This process takes place successively at localized volumes in the wire (see Fig. 7), resulting in stress fluctuations on the upper stress plateau when measured over the whole wire length. Its reproducibility for eight cycles (see Fig. 4(b)) can be attributed to reorientation process taking place in various segments following a fixed sequence, probably reflecting different crystallographic orientations (and thus critical resolved stress to induce twinning) with respect to the applied stress.

As reviewed earlier, Qian et al. [16] and Zhang et al. [17] reported superelasticity in autenitic Ni-Mn-Ga wires by stress-induced martensitic-austenitic transformations on loading and unloading, and we reported superelastic behavior in Ni-Mn-Ga wires by reversible intermartensitic transformation [19]. By contrast, in the present work, we show that superelasticity is due to reversible martensitic variant reorientation without crystallographic transformation, albeit in a Ni-Mn-Ga wire which is richer in nickel than the above ones. Generally, the detwinning process or variants reorientation observed in Ni-Mn-Ga is expected to be irreversible on unloading, thus creating a permanent plastic deformation mechanism. Thus, we believe that the reversible (de)twinning on (un)loading is due to internal stresses generated by the motion of twin boundaries in the presence of non-twinning obstacles, i.e.,the $\gamma$ precipitates. A similar hypothesis was advanced to explain the ~4% recovery observed in a 5M Ni-Mn-Ga single crystal, where obstacles to the twins were attributed the rough surface of the sample [29]. Thus, we believe that the superelastic behavior of the present wires can be attributed to the existence of the $\gamma$ precipitates (and possibly also surface roughness), creating incompatibility stresses during detwinning on loading, which are relaxed on unloading by reversible twinning, leading to full strain recovery and a reproducible sequence of twinning events on subsequent load-unload loops, thus explaining the reproducible shape of the superelastic plateaus.

### 4.3 Effect of temperature on tensile behavior

It has been known in Fig. 4 that the twinning stress decreases with increasing temperature. Also, the lattice parameters change monotonously, as does the twinning

stress, when decreasing temperature, as shown in Fig. 8. We hypothesize that the temperature dependence of the twinning stress is linked to the anisotropic thermal expansion and the increase of tetragonality with decreasing temperature, which increases the mismatch between variants in different orientation and makes it more difficult to trigger the twinning process as temperature drops. Similar results have been reported for monocrystalline 5M modulated martensite for which the twinning stress increases approximately linearly with decreasing temperature for Type I twins [30-31]. In addition, the reason for the discontinuity at 47 ºC for the temperature dependence of $\Delta a/a$ and $\Delta c/c$ remains unknown, which needs further study.
xxx

## 5. Conclusions

A Ni-Mn-Ga microwire was prepared by the Taylor method, consisting of bamboo grains with a tetragonal martensite matrix and coarse γ phase precipitates. The wire exhibits superelastic behavior with reproducible fluctuations on the upper stress plateau during uniaxial tensile tests at ambient temperature. In-situ synchrotron X-ray diffraction experiments reveal that superelasticity is due to reversible variants reorientation (i.e., (de)twinning), with lattice rotation, occurring consecutively in various segments of the wire during loading and unloading, which results in reproducible fluctuations in the stress plateau. The recovery during unloading (i.e., superelasticity) is attributed to the internal stresses created by the detwinning martensite in the presence of the non-twinning precipitates. The plateau stress increases with decreasing temperature from 55 to –70 ºC and this temperature dependence is related to the change of unit cell tetragonality with temperature, as measured by X-ray diffraction.

## Acknowledgments

This research was supported by the US National Science Foundation through Grant No. DMR-1207282 at Northwestern University (Z.L.W. and D.C.D.), the National Basic Research Program of China (973 Program) under Contract No. 2012CB619405 (Z.H.N. and Y.D.W.) at Beijing Institute of Technology, and Grant No. DMR-1207192 at Boise State University (P.M.). Z.L.Wang also thanks the support from the Chinese Scholarship Council (CSC). Use of the Advanced Photon Source was supported by the U.S. Department of Energy, Office of Science, Office of Basic Energy Science, under Contract No. DE-AC02-06CH11357. We thank Dr. Cun Yu for the assistance during experiments in APS and Prof. L.C. Brinson at Northwestern University for use of her dynamical mechanical analysis instrument.

## References


[1] Murray SJ, Marioni M, Allen SM, O'Handley RC, Lograsso TA. Appl Phys Lett 2000;**77**:886.
[2] Sozinov A, Likhachev AA, Lanska N, Ullakko K. Appl Phys Lett 2002;**80**:1746.
[3] Sozinov A, Lanska N, Soroka A, Zou W. Appl Phys Lett 2013;**102**:021902.
[4] Gaitzsch U, Pötschke M, Roth S, Rellinghaus B, Schultz L. Acta Materialia 2009;**57**:365.
[5] Dunand DC, Müllner P. Adv Mater 2011;**23**:216.
[6] Scheerbaum N, Heczko O, Liu J, Hinz D, Schultz L, Gutfleisch O. New J Phys 2008;**10**:073002.
[7] Chmielus M, Zhang XX, Witherspoon C, Dunand DC, Müllner P. Nature Materials 2009;**8**:863.
[8] Gomez-Polo C, Perez-Landazabal JI, Recarte V, Sanchez-Alarcos V, Badini-Confalonieri G, Vazquez M. J Appl Phys 2010;**107**:123908.
[9] Zhukova V, Rodionova V, Fetisov L, Grunin A, Goikhman A, Torcunov A, Aronin A, Abrosimova G, Kiselev A, Perov N. IEEE Trans Magn 2014;**50**:2505504.
[10] Zhukov A, Rodionova V, Ilyn M, Aliev AM, Varga R, Michalik S, Aronin A, Abrosimova G, Kiselev A, Ipatov M, Zhukova V. J Alloy Compd 2013;**575**:73.
[11] Rodionova V, Ilyn M, Granovsky A, Perov N, Zhukova V, Abrosimova G, Aronin A, Kiselev A, Zhukov A. J Appl Phys 2013;**114**:123914.
[12] Aronin AS, Abrosimova GE, Kiselev AP, Zhukova V, Varga R, Zhukov A. Intermetallics 2013;**43**:60.
[13] Zhukov A, Garcia C, Ilyn M, Varga R, del Val JJ, Granovsky A, Rodionova V, Ipatov M, Zhukova V. J Magn Magn Mater 2012;**324**:3558.
[14] Varga R, Ryba T, Vargova Z, Saksl K, Zhukova V, Zhukov A. Scripta Mater 2011;**65**:703.
[15] Zhukova V, Ipatov M, Granovsky A, Zhukov A. J Appl Phys 2014;**115**:17A939.
[16] Qian MF, Zhang XX, Witherspoon C, Sun JF, Müllner P. J Alloy Compd 2013;**577, Supplement 1**:296.
[17] Zhang Y, Li M, Wang YD, Lin JP, Dahmen KA, Wang ZL, Liaw PK. Adv Eng Mater 2014;**16**:955.
[18] Liu Y, Zhang X, Xing D, Shen H, Chen D, Liu J, Sun J. Phys Status Solidi A 2015;**212**:855.
[19] Zheng P, Kucza NJ, Patrick CL, Müllner P, Dunand DC. J Alloy Compd 2015;**624**:226.
[20] Kucza NJ, Patrick CL, Müllner P, Dunand DC. Submitted for publication 2015.
[21] Mahnke GJ, Seibt M, Mayr SG. Physical Review B 2008;**78**:012101.
[22] Ma Y, Jiang C, Li Y, Xu H, Wang C, Liu X. Acta Mater 2007;**55**:1533.
[23] Toby BH. J Appl Crystallogr 2001;**34**:210.
[24] Pond RC, Muntifering B, Müllner P. Acta Mater 2012;**60**:3976.
[25] Zárubová N, Ge Y, Heczko O, Hannula SP. Acta Mater 2013;**61**:5290.
[26] Muntifering B, Pond RC, Kovarik L, Browning ND, Müllner P. Acta Mater 2014;**71**:255.

[27] Nie ZH, Ren Y, Terai T, Wang YD, Brown DE, Kakeshita T. Appl Phys Lett 2009;**95**:051914.
[28] Straka L, Heczko O, Seiner H, Lanska N, Drahokoupil J, Soroka A, Fähler S, Hänninen H, Sozinov A. Acta Materialia 2011;**59**:7450.
[29] Chmielus M, Witherspoon C, Ullakko K, Müllner P, Schneider R. Acta Mater 2011;**59**:2948.
[30] Glavatska N, Mogylny G, Glavatskiy I, Gavriljuk V. Scripta Mater 2002;**46**:605.
[31] Straka L, Soroka A, Seiner H, Hänninen H, Sozinov A. Scripta Mater 2012;**67**:25.

Figure Captions

Fig.1 Schematic illustration of setup for in-situ X-ray diffraction experiment.

Fig. 2 SEM micrographs of (a) wire, (b) fracture surface and (c-e) optical micrographs of (c) radial and (d-e) longitudinal cross-sections, showing martensite (M) plates, precipitates (γ) and surface cavities (H). The dotted lines correspond to the direction of the martensite plates.

Fig. 3 Diffraction patterns for segments 3 and 10, with and without γ phase detected. The subscripts of P, γ and T denote parent (austenitic) phase, γ phase and tetragonal martensite.

Fig. 4 Tensile stress-strain curves for (a) three maximum applied strain at ambient temperature, (b) a constant maximum applied strain of 2% at ambient temperature, (c) constant maximum applied strain of 2% at various temperatures and (d) dependence of twinning stress from (c) on the temperature over the range of -70 to 55 ℃. The curves are shifted along strain axis to facilitate comparisons in (b) and (c).

Fig. 5 Tensile stress-strain curve recorded during in-situ x-ray experiments (no continuous load data on loading from 0 to 0.83%). The red squares correspond to the strain values where diffraction patterns were collected on fifteen segments (marked 1-15 on the wire schematic on the left) covering the whole gauge length of the wire.

Fig. 6 Diffraction patterns for segments 7-10 before loading, at the maximum applied strain and after unloading.

Fig. 7 Diffractions pattern for segments 7-10 at different applied loading strains with change in patterns highlighted with colored boxes.

Fig. 8 Temperature dependence during cooling from 177 to 27 ℃ of (a) lattice parameter thermal strain of tetragonal unit cell (b) volumetric strain and tetragonality of unit cell.

Fig. 9 (a) Diffraction patterns indexed with three kinds of variants before loading (left) and at the maximum applied strain (right). (b) Schematic for the lattice rotation and variants reorientation at the atomic scale.

Figures:

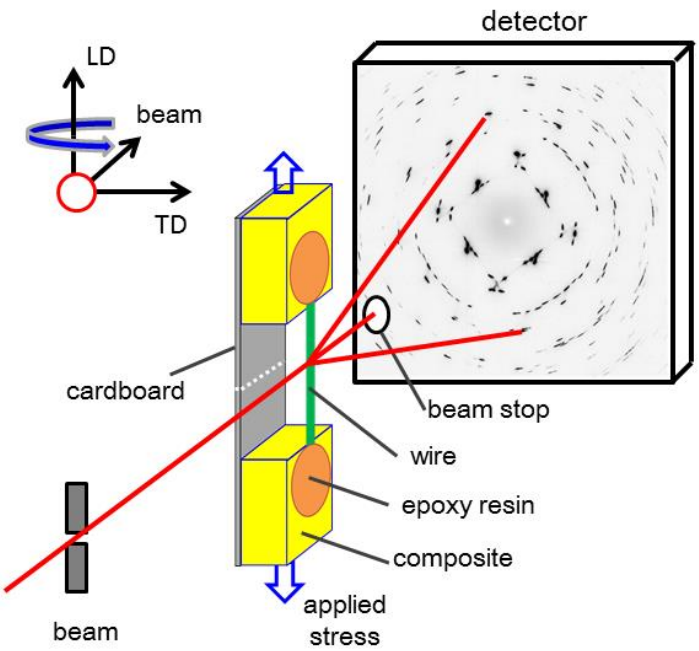


Fig.1 Schematic illustration of setup for in-situ X-ray diffraction experiments

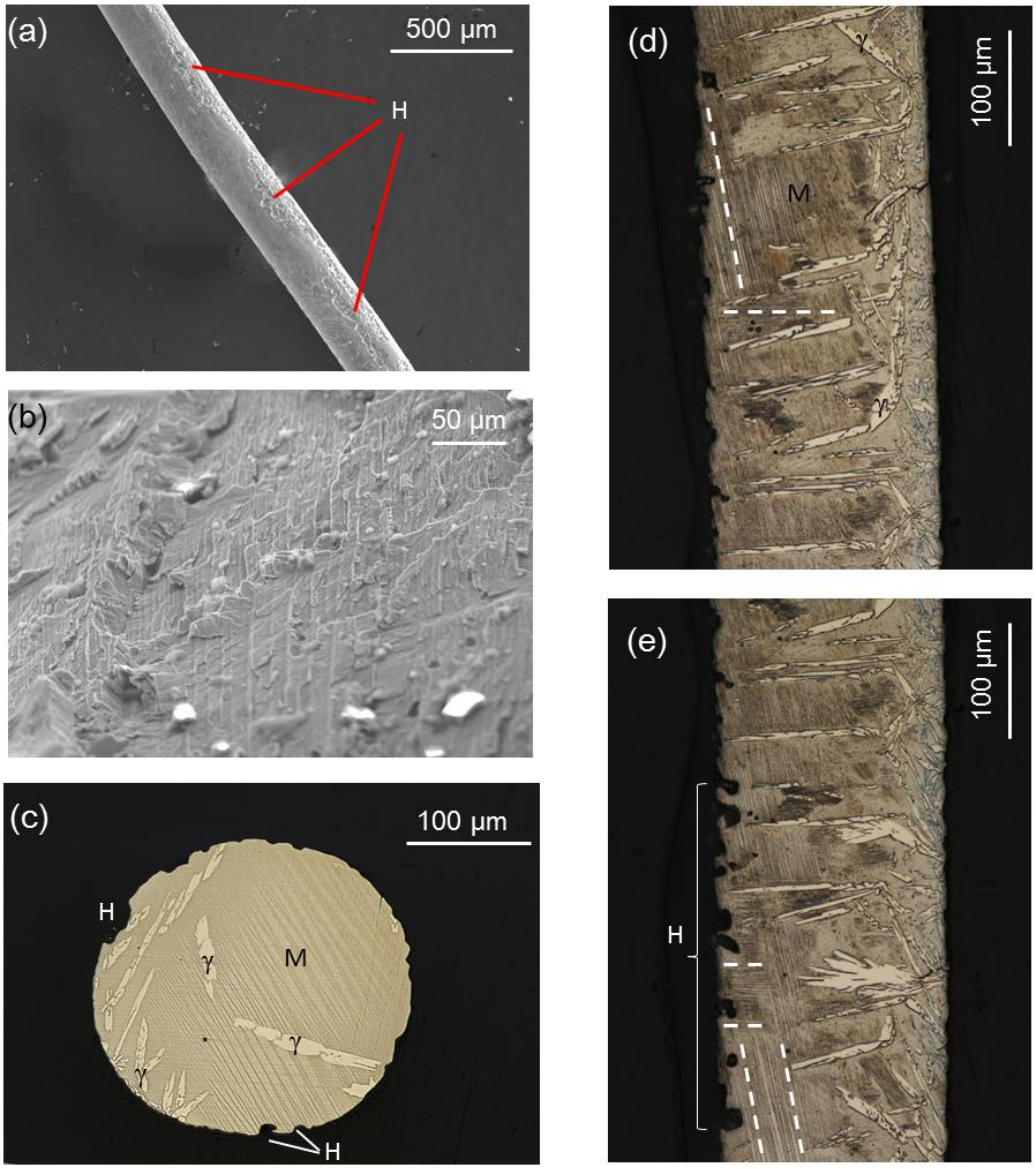


Fig. 2 SEM micrographs of (a) wire, (b) fracture surface and (c-e) optical micrographs of (c) radial and (d-e) longitudinal cross-sections, showing martensite (M) plates, precipitates (γ) and surface cavity (H). The dotted lines correspond to the direction of the martensite plates.

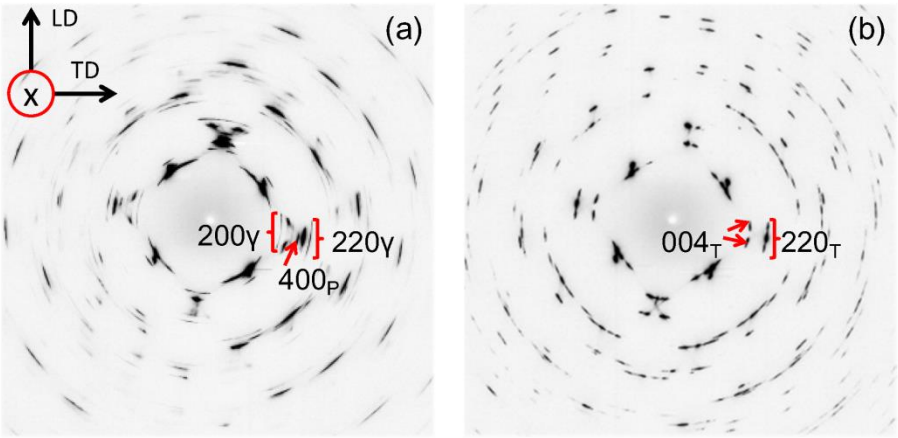


Fig. 3 Diffraction patterns for segments 3 and 10, with and without γ phase detected. The subscripts of P, γ and T denote parent phase, γ phase and tetragonal martensite.

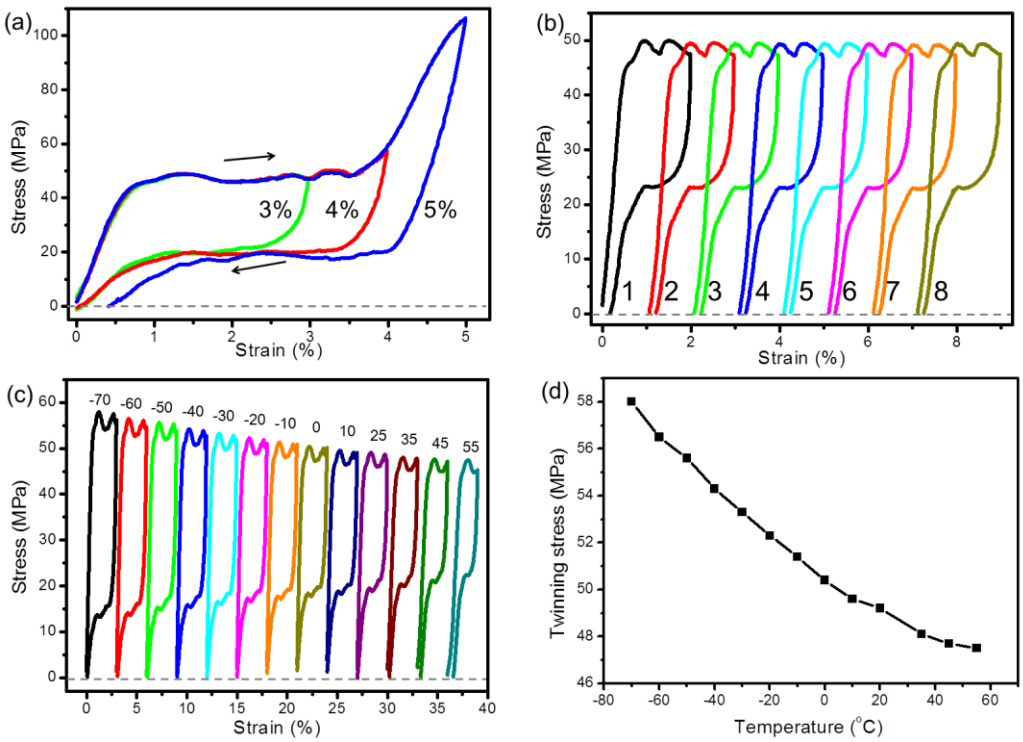


Fig. 4 Tensile stress-strain curves for (a) three maximum applied strain at ambient temperature, (b) a constant maximum applied strain of 2% at ambient temperature, (c) constant maximum applied strain of 2% at various temperatures and (d) dependence of twinning stress from (c) on the temperature over the range of -70 to 55 ℃. The curves are shifted along strain axis to facilitate comparisons in (b) and (c).

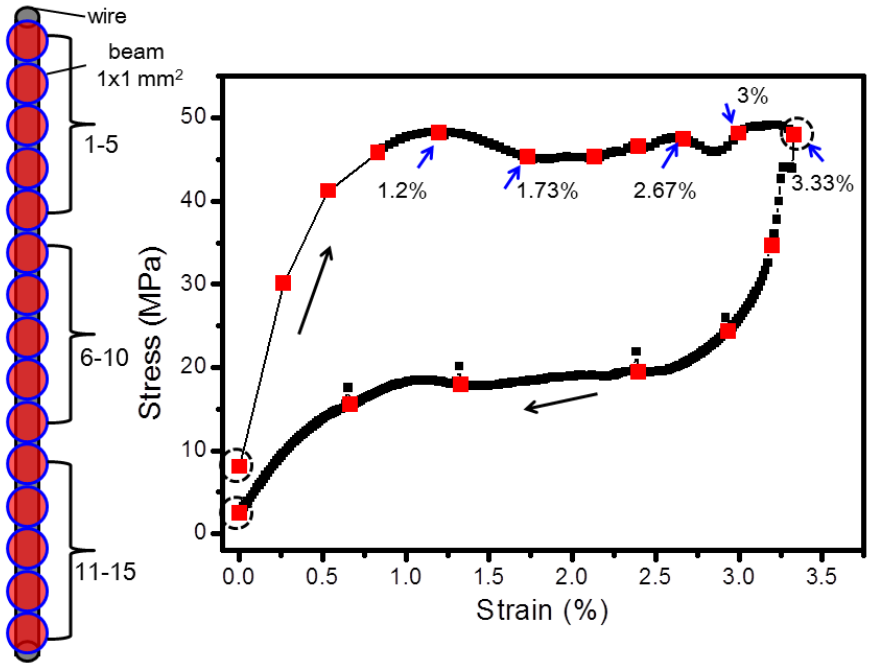


Fig. 5 Tensile stress-strain curve recorded during in-situ x-ray experiments (no continuous load data on loading from 0 to 0.83%). The red squares correspond to the strain values where diffraction patterns were collected. Fifteen segments (marked 1-15 on the wire schematic on the left) covering the whole gauge length of the wire.

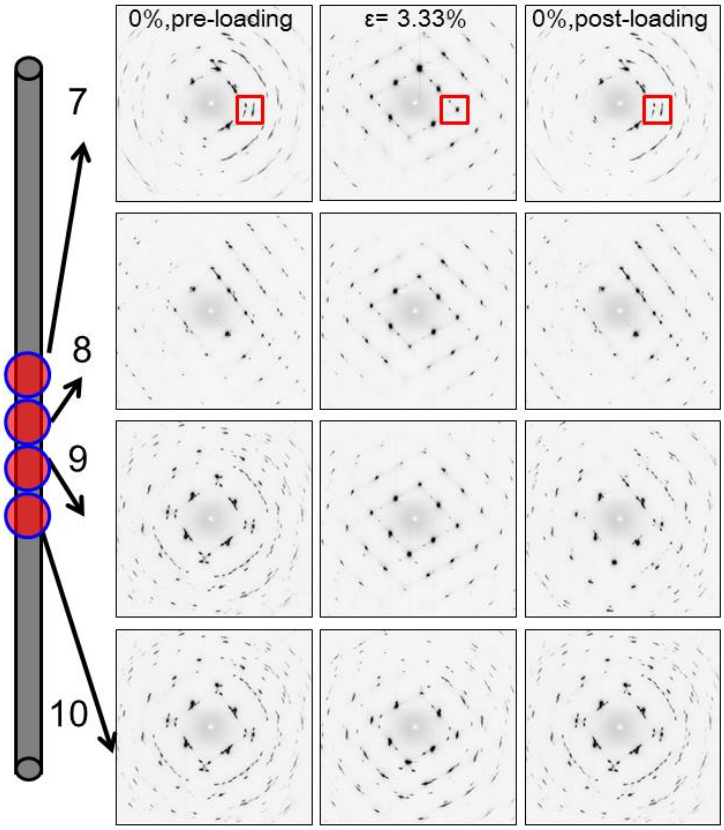


Fig. 6 Diffraction patterns for spot 7-10 before loading, at the maximum applied strain and after unloading.

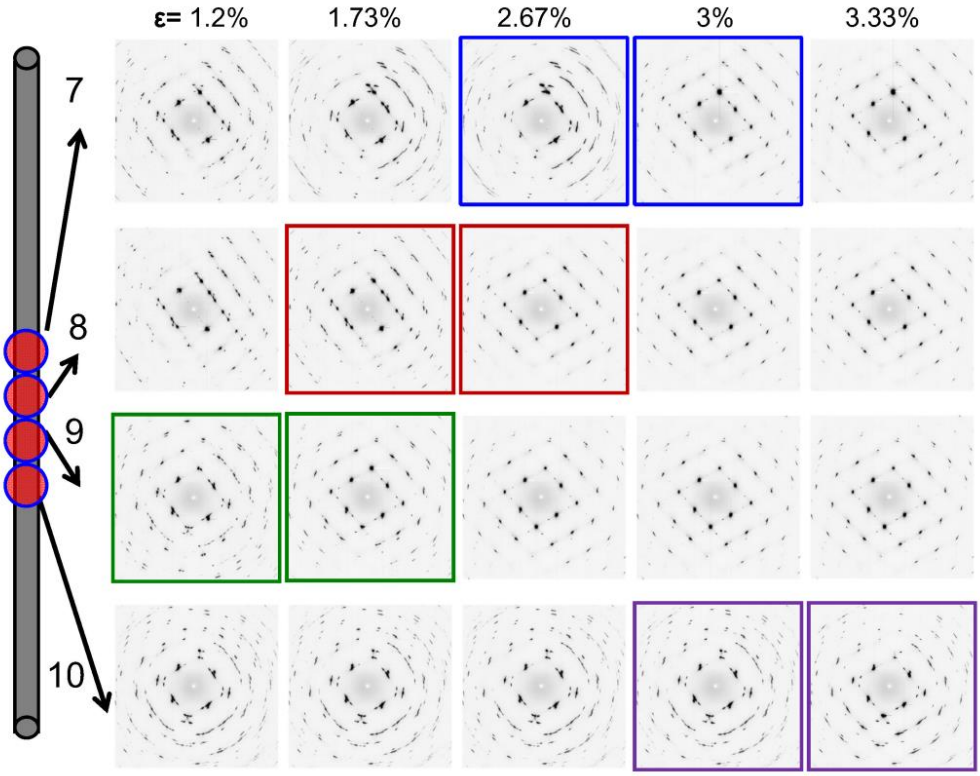


Fig. 7 Diffractions pattern for segments 7-10 at different applied loading strains with change in patterns highlighted with colored boxes.

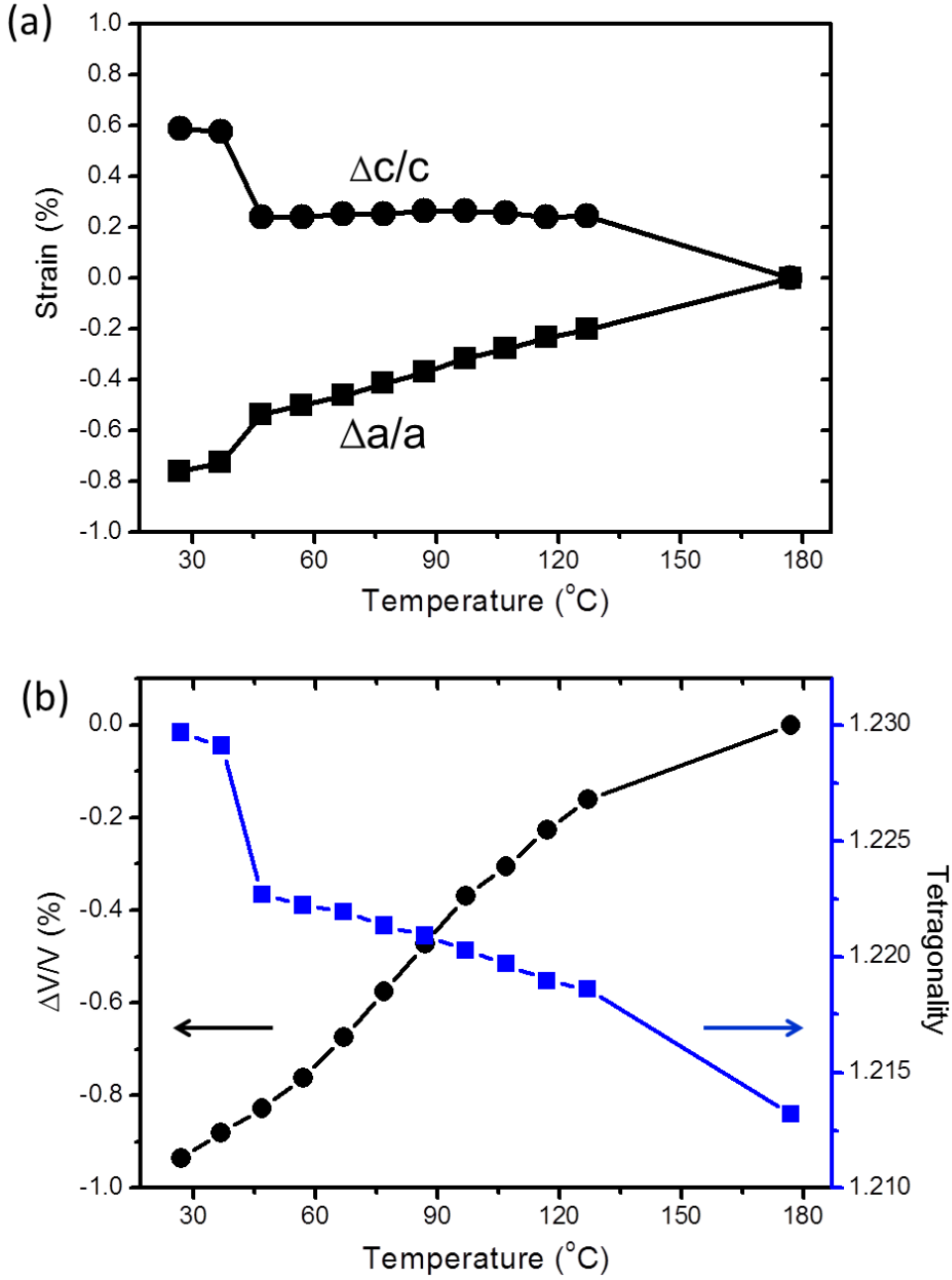


Fig. 8 (a) Temperature dependence during cooling from 177 to 27 ºC of (a) lattice parameter thermal strain of tetragonal unit cell (b) volumetric strain and tetragonality of unit cell.

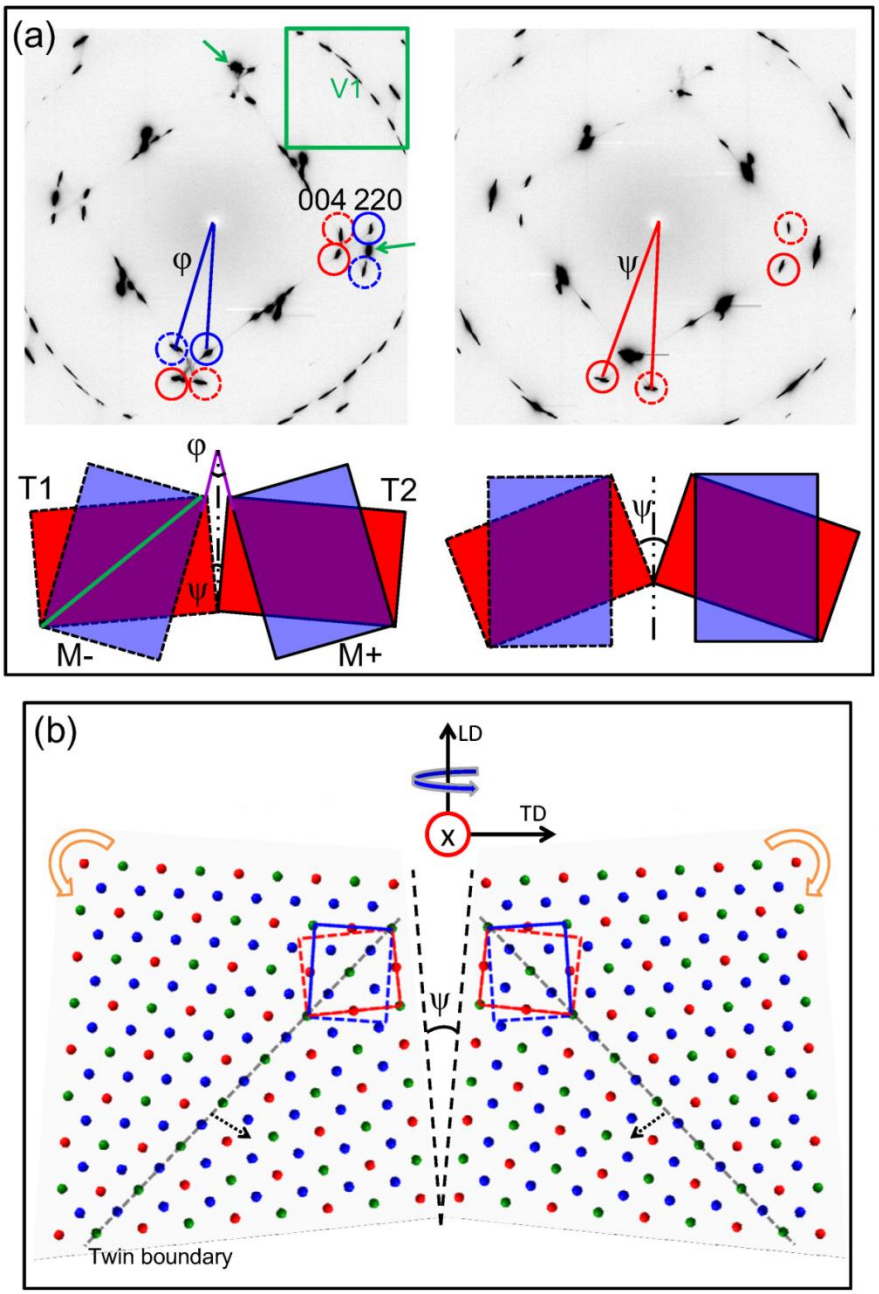


Fig. 9 (a) Diffraction patterns indexed with three kinds of variants before loading (left) and at the maximum applied strain (right). (b) Schematic for the lattice rotation and variants reorientation at the atomic scale.